Catalysis Science & Technology

ROYAL SOCIETY OF CHEMISTRY

PAPER

View Article Online
View Journal | View Issue

Cite this: *Catal. Sci. Technol.*, 2026, **16**, 1444

Operando X-ray absorption spectroscopy of phosphomolybdic acid redox mediators for electrochemical conversion of biomass to green hydrogen

Robert Price, †[a] Lewis MacDonald, †[a] Luke L. Keenan, †[b] William Johnson,[a] Stephen M. Lyth,[a] Jun Li[a] and Edward Brightman *[a]

Green hydrogen production is limited by the thermodynamic energy requirement of water splitting. By decoupling the anodic and cathodic reactions using redox mediators, alternative feedstocks such as lignocellulosic biomass can yield comparable hydrogen purity with around half the total electrical energy input of conventional water electrolysis. Keggin-type heteropolyacids such as phosphomolybdic acid ($H_3PMo_{12}O_{40}$) are increasingly of interest as mediators in decoupled electrochemical energy conversion applications, due to their reversible redox characteristics. However, the redox behaviour of heteropolyacids in aqueous solution during this process is still poorly understood. X-ray absorption spectroscopy (XAS) techniques offer the opportunity to directly probe changes in oxidation state and local structure of the mediator *in operando*, allowing unprecedented insight into redox processes in a flow cell environment. Here, for the first time, we demonstrate *operando* XAS of reduced phosphomolybdic acid as it undergoes oxidation in a proton exchange membrane electrolyser with bespoke 3D-printed flow-fields. Changes in the time-resolved XAS were correlated to structural changes in the Keggin anion, which were closely related to the state-of-charge of the mediator, laying the groundwork for future studies of solution-phase Keggin-type heteropolyacid redox states. Furthermore, reduction of the phosphomolybdic acid *via* mild thermal digestion of either pure lignin or real agricultural biowaste is compared, in a step towards real-world applications. This work contributes significantly to the efficient and low-cost production of green hydrogen from waste biomass feedstocks, as well as providing insights into similar decoupled electrolysis processes.

Received 24th June 2025,
Accepted 15th January 2026

DOI: 10.1039/d5cy00763a

rsc.li/catalysis

1. Introduction

Hydrogen is central to decarbonising hard-to-abate sectors and enabling sustainable chemical synthesis. Today, most hydrogen is produced *via* steam reforming of natural gas, generating substantial CO_2 emissions.[1] Green hydrogen from water electrolysis offers a low-carbon alternative, but conventional systems remain costly due to high cell voltages and reliance on scarce catalysts such as iridium, to overcome the sluggish oxygen evolution reaction which consumes around one quarter of the energy required for the process, and 30–50% of stack manufacturing costs.[2–4]

Decoupled electrolysis provides a promising route to hydrogen with lower energy input and cost by separating oxidation and reduction steps using a soluble redox mediator such as a polyoxometalate (POM), and can make use of sustainable feedstocks such as waste biomass instead of pure water.[5] This eliminates the need for an oxygen evolution reaction (OER) catalyst at the anode and enables operation at lower cell voltages. In such a system, the mediator is reduced chemically through interaction with a low-value feedstock such as lignocellulosic biomass. The reduced mediator can then be oxidised electrochemically to generate hydrogen (taking the place of water in a conventional electrolyser).[6,7] The regenerated mediator can be cycled in either a batch or continuous system.[8] This architecture significantly improves the system design not only by removing the need for expensive OER catalysts, but also by drastically reducing energy input because the thermodynamic and kinetic barriers associated with water oxidation are bypassed; hence cell voltages are lowered from ~1.6 V, for a typical commercial PEM water electrolyser, to between 0.8 V and 1.0 V. Furthermore, the flow cell design

[a] *Strathclyde Incubator for Green Hydrogen Technologies (SigH$_2$t), Department of Chemical and Process Engineering, University of Strathclyde, James Weir Building, 75 Montrose Street, Glasgow, G1 1XJ, UK. E-mail: edward.brightman@strath.ac.uk*
[b] *Diamond Light Source Ltd., Harwell Science and Innovation Campus, Fermi Avenue, Didcot, OX11 0DE, UK*
† These authors share equal first authorship.

enables continuous operation and precise control of the reaction environments, making decoupled electrolysis a scalable and potentially more energy-efficient pathway for green hydrogen production.

Mediator selection is critical to the performance of decoupled electrolysis. In this work, we focus on POMs, which comprise large polyanions based upon $[MO_x]_n$ units (M = Mo, W, V or Nb and x = 4–7) with various charge-balancing cations.[9] One branch of POMs which are particularly well-studied as electrocatalysts/mediators are heteropolyanion (HPA) POMs in which a heteroatom (*e.g.* phosphorous) lies at the centre of the POM cluster.[9–13] HPAs include Dawson-type ($[X_2M_{18}O_{62}]^{4-}$) and Keggin-type ($[XM_{12}O_{40}]^{3-}$) structures (X = heteroatom), both capable of multiple highly reversible one- or two-electron reductions.[9,13]

Keggin-type POMs, such as phosphomolybdic acid ($H_3[PMo_{12}O_{40}]$ or PMA), have shown good thermal and redox cycling stability during electrochemical evaluation, and readily react with lignin and cellulose, making them promising candidates for use as mediators in the aforementioned biomass digestion and electrolysis process.[14–21] As such, $H_3[PMo_{12}O_{40}]$ has been the primary mediator used in a number of studies of this type. For example, Liu *et al.* performed thermal and UV-irradiative digestion of lignin, cellulose, starch and glucose, prior to electrolysis using a PEM electrolysis cell. Using a PGM-free carbon cloth anode, a Nafion PEM and a Pt/C cathode, hydrogen production was achieved with an electricity consumption as low as 0.69 kWh N m^{-3}.[20] Li *et al.* also found that significant reductions in power consumption in the production of hydrogen from corn starch could be made using a similar process (in comparison to water electrolysis using a PEM electrolyser).[18]

Deeper understanding of the processes occurring in decoupled electrolysis systems may ultimately lead to improved performance by informing tailored formulation of heteropolyacid mediators and operating conditions. One powerful tool to probe the chemical state of materials systems is X-ray absorption spectroscopy (XAS). XAS analyses of various POM mediators have been performed previously, but those concerning $H_3[PMo_{12}O_{40}]$ focus primarily on *ex situ* analysis[22–27] and some *in situ* studies,[28,29] all in the solid state. Most relevant to the aforementioned aqueous-phase electrolysis of $H_3[PMo_{12}O_{40}]$ is an *operando* report of the use of $TBA_3[PMo_{12}O_{40}]$ (TBA = $[N(CH_2CH_2CH_2CH_3)_4]^+$) as a cathode material for lithium-ion batteries (LIBs). XAS of this cathode material upon charging and discharging clearly demonstrates the reversible structural changes of this heteropolyanion induced by the transformation of a Mo═O bond to a Mo–O bond.[30]

However, operando XAS in the aqueous phase for POM-based systems remains largely unexplored and presents unique challenges. Unlike solid-state studies, aqueous-phase measurements require handling highly absorbing liquid samples within an electrochemical environment, maintaining stable flow and avoiding beam-induced artefacts. Additionally, the dynamic redox behaviour of POMs in solution under applied potential introduces complexity in correlating spectral changes to electrochemical states. Furthermore, designing an electrochemical cell that is simultaneously suitable for operando XAS measurements and efficient for electrolysis is highly complex, requiring specialized materials and construction. Despite these challenges, such studies are highly valuable: they provide direct insight into the structural and electronic evolution of mediators under realistic operating conditions, enabling mechanistic understanding that cannot be captured *ex situ*.

Recently, we reported the successful electrochemical conversion of whisky distillery waste streams (draff, pot ale and spent lees) to hydrogen *via* thermal digestion with a 0.3 mol dm^{-3} solution of $PMA_{(aq)}$ followed by PEM electrolysis using a carbon felt anode and a Pt/C cathode with a loading of only 0.937 mg cm^{-2} Pt.[15] While biomass conversion was demonstrated, limitations in materials and setup prevented high faradaic efficiencies.

Here, we present the first operando XAS investigation of PMA during aqueous-phase electrolysis, using a bespoke PEM electrolysis cell enabling simultaneous XAS, electrochemical monitoring, and gas analysis. We compare PMA solutions reduced electrochemically and *via* biomass digestion, correlating Mo K-edge spectral changes with state-of-charge and hydrogen production measured by mass spectrometry during electro-oxidation, towards a deeper understanding of reversible redox behaviour of POM mediators in decoupled electrolysis applications.

2. Experimental

2.1 Preparation of reduced phosphomolybdic acid solutions

2.1.1 Thermogravimetric analysis. Samples of phosphomolybdic acid ($H_3[PMo_{12}O_{40}]\cdot xH_2O$, PMA, Thermo Scientific Chemicals, ACS Reagent) were subjected to thermogravimetric analysis (TGA) using a Netzsch STA 449 C Jupiter ® instrument (University of St Andrews) and a Netzsch STA 449 F3 Jupiter® instrument (University of Strathclyde) to determine the water content of the as-received material. Firstly, a correction run using two empty alumina crucibles (one for reference and one for sample) was performed by heating the furnace to 600 °C at a rate of 5 °C min^{-1} under a 20 cm^3 min^{-1} flow of compressed air. Subsequently, PMA was added to the sample crucible and analysed using the same method, subtracting the correction run from the experimental data using the Netzsch Proteus analysis software. Run 1 (University of St Andrews) employed 90.49 mg of PMA, whilst runs 2 and 3 (University of Strathclyde) used 81.00 mg and 75.83 mg, respectively. The water content determined was then used to produce PMA solutions of known concentration.

2.1.2 Cyclic voltammetry and electrochemical reduction/oxidation of PMA. Electrochemical behaviour of the PMA solution was thoroughly characterised *ex situ* to provide a baseline for analysing the biomass electrolysis process. 500 cm^3 of stock solution of 0.1 mol dm^{-3} PMA was prepared by dissolving the yellow, crystalline material in deionised water (DI H_2O, 15.0 MΩ cm) under stirring at 25 °C. The requisite

mass was determined from the TGA analysis described above.

Cyclic voltammetry and bulk electrolysis experiments of aliquots of this solution were performed using a BioLogic SP300 potentiostat with a Ag/AgCl reference electrode (conditioned in 3.0 mol dm^{-3} $KCl_{(aq)}$) and a coiled platinum wire counter electrode. For publication the potential data have been converted to the reversible hydrogen electrode (RHE) scale based on the measured PMA solution pH = 0.8 and using the formula E(V *vs.* RHE) = E(V *vs.* Ag/AgCl) + 0.209 (V) + 0.059 × pH (V). For cyclic voltammetry the working electrode was a glassy carbon disk (area 0.071 cm^2) in an unstirred single chamber cell with PMA diluted to 0.01 mol dm^{-3}. For bulk electrolysis experiments an H-cell was used, with a platinum wire working electrode. Both the compartments were stirred and separated by an activated Nafion™ 117 membrane. For the reduction step, the working compartment contained 15 cm^3 of 0.1 mol dm^{-3} PMA, while the counter compartment contained 15 cm^3 of 0.5 mol dm^{-3} H_2SO_4. Bulk reduction of the PMA was performed using a chronoamperometric method at a constant potential of 0.506 V *vs.* RHE until the theoretical amount of charge required to reduce this volume of $PMA_{(aq)}$ by 2 electrons had been passed and the current began to plateau. Results from an example of this process are shown in Fig. S4a, together with oxidation of the same solution sample at 0.947 V *vs.* RHE, shown in Fig. S4b. For further experiments and comparisons, the remaining volume of the stock solution was fully reduced until the theoretical amount of charge required for 2 electron reduction had been achieved, subsequently referred to as "electrochemically reduced" herein.

2.1.3 Thermal digestion of biomass. Separate 100 cm^3 solutions of $PMA_{(aq)}$ were prepared to 0.1 mol dm^{-3} concentration for digestion of biomass, as an alternative method of reducing the mediator. 25 cm^3 of the $PMA_{(aq)}$ solution was added to a three-neck, 25 cm^3 round bottom flask, along with a magnetic stirrer (setup shown in Fig. 1). Subsequently, the biomass source was added to a (dry basis) concentration of 30 g dm^{-3}. Two types of biomass were trialled in this study: lignin (alkali, Sigma-Aldrich) and draff from the Isle of Raasay Distillery. Draff comprises the spent barley grains from the whisky production process and further details of its characterisation may be found in our previous publication.[15] The flask was connected to a reflux condenser *via* the central neck, whilst the remaining necks were used to introduce a continuous purge of Ar (100 cm^3 min^{-1}) (to ensure anaerobic conditions) and a thermocouple (to monitor reaction temperature). The flask was lowered into a silicone oil heating basin resting on a hotplate stirrer and the purge of Ar was initiated to flush the system for 10 minutes. Subsequently, the temperature of the hotplate was increased to 160 °C (corresponding to a reaction temperature of 100 °C) and stirring of both the silicone oil and the reaction mixture at 800 rpm commenced. Once the reaction mixture had stabilised at 100 °C, typically after 20 to 30 minutes, the reaction was allowed to proceed for 4 hours before cooling. The cooled mixture changed from transparent yellow to dark blue in colour and was Buchner filtered to remove any solid residues of biomass.

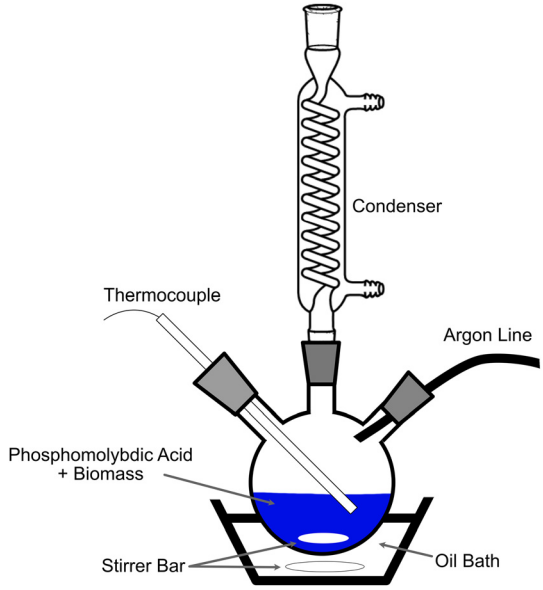

Fig. 1 Thermal digestion setup employed for waste biomass digestion used to reduce the PMA catalyst.

2.2 Proton exchange membrane electrolyser

A flow cell setup was used to re-oxidise reduced PMA solutions using a proton exchange membrane electrolysis cell (PEMEC). The flow cell design is from Pinflow energy storage (Czech Republic), however some custom components were manufactured to allow for operando X-ray absorption spectroscopy (XAS). Fig. 2a shows an overview of the components used to construct the flow cell. From the outside towards the centre, the flow cell comprised customised 22 mm thick Al end plates, PTFE insulating sheets (0.2 mm thickness) and Cu current collection plates (2 mm thickness) with a 10 mm diameter central aperture to allow transmission of the focussed X-ray beam through the cell (Fig. 2b). Next, conductive carbon plates and 3D-printed plastic flow frames were stacked together to complete one half of the flow cell. This stacking process was identical for each side of the setup. As the anolyte and catholyte liquids were introduced to the PEMEC through the plastic flow frames, silicone gaskets were applied to the faces of these flow frames to prevent leakage around the PEMEC. The flow frames (Fig. 2c) contained rectangular apertures of 40 mm × 50 mm area which were used to feed the electrolytes into the anode and cathode chambers. 5 mm thick carbon felt electrodes/current collectors are placed into these apertures in direct contact with the carbon plates.

A non-activated carbon felt (Mersen, Scotland) was employed as the anode material whilst an activated carbon felt was employed as the cathode current collector. In addition, a gas diffusion electrode (GDE) containing a HyPer™ Pt black catalyst (0.4 mg cm^{-2}) on carbon paper from Ames Goldsmith Ceimig Ltd. (Dundee, Scotland) was employed as a hydrogen evolution

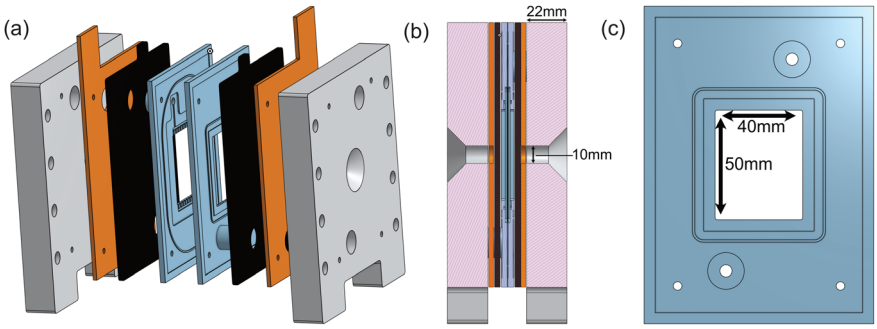

Fig. 2 a) Exploded view of the bespoke PEM electrolysis cell, b) cross section of constructed cell with 10 mm diameter bore to allow transmission of X-rays during XAS experiments, c) flow field plate with 20 cm^2 working area.

reaction (HER) catalyst on the cathode side. A Nafion™ 117 proton exchange membrane (PEM) was applied to the silicone gasket on the cathode side of the setup, isolating the cathode and anode compartments, when final stacking of the anode side onto the cathode side was complete, to form the membrane electrode assembly (MEA). The setup was secured and compressed with nuts and bolts tightened to a torque of 9 N m using a calibrated torque screwdriver.

30 cm^3 of the anolyte (0.1 mol dm^{-3} reduced PMA) and catholyte (0.5 mol dm^{-3} $H_2SO_{4(aq)}$) solutions were placed into two separate 50 cm^3 Duran bottles fitted with GL32 3-port connector caps. Silicone tubes were attached to the inlet and outlet ports for circulation of the electrolytes between the reservoirs and the flow cell electrode compartments through a Masterflex™ L/S™ Digital Miniflex Pump (Dual Channel), fitted with L/S™ 16 Tygon™ tubing. The final port from the reservoirs was used to allow gas collection or analysis. For operando XAS experiments a 2-electrode setup was used with the cell potential difference measured as described in section 2.3.3. To further illustrate the anode potential profile during the oxidation step, a flow cell was also set up with a reference electrode for the result shown in Fig. 3c. Here, a Hydroflex hydrogen reference electrode was placed in a separate beaker of 0.5 mol dm^{-3} H_2SO_4 which was physically connected to the inlet tube on the anode side *via* a piece of activated Nafion™ tubing. The tubing was activated in a comparable manner to the Nafion™ 117 membrane. The measured potentials in this experiment have been converted to RHE using the PMA solution pH = 0.8, *i.e.* +47.2 mV.

2.3 *Operando* X-ray absorption spectroscopy

2.3.1 XAS experimental conditions. XAS experiments were performed at beamline B18 (core EXAFS) at Diamond Light Source (Didcot, United Kingdom).[31] The aforementioned flow cell setup was mounted onto the motorised stage (SI, Fig. S1) and electrical connections were made to a Metrohm Autolab PGSTAT204 (with a FRA32M frequency response analyser) for electrochemical analysis.

At the time of the measurements the synchrotron was operating with a ring energy of 3 GeV and at a current of 300 mA. The X-ray source was a bending magnet and, *via* a pair of Si(111) DCM crystals, with focussing Si mirrors coated in Pt pitched at 2.4 mrad, the beamline delivers an X-ray spot size of 800 × 800 μm^2 FWHM (V × H) to the sample position. The data were acquired in transmission mode using ion chambers and Stanford amplifiers. Acquisition times of 31.55 s per spectrum were used in QEXAFS mode with ~8.2 ms per point and a 0.3 eV step size. The energy calibration of the DCM was achieved by measuring the spectrum of a Mo foil.

Pellets of standard materials were prepared by adding the required mass of material to cellulose (Sigma-Aldrich), totalling 80 mg, and thoroughly mixing in a pestle and mortar to ensure homogeneity. The mixture was subsequently pressed in a 13 mm diameter die and punch at 1 tonne for 60 seconds. Pellets were transferred to a sample frame and held in place with Kapton tape at the edges, before being mounted on the B18 beamline for XAS analysis of the Mo K-edge. A summary of the full list of materials and masses used to create standard pellets is included in SI, Table S1. Table 1 lists the relevant quantities used for MoO_3 and MoO_2 pellets. In addition, a Mo foil standard sample was also used (25 μm foil thickness, 99.9% purity, Goodfellow, UK).

2.3.2 XAS analysis. Data processing of the spectra was performed using Athena v 0.9.26, part of the Demeter software[32] and followed standard procedures. The cyclic X-ray absorption spectra were processed with the Diamond Light Source developed DAWN program v. 2.22.[33] A deglitching and normalisation processing followed this step. The k^2-weighted EXAFS spectra underwent Fourier transform over the k = 3.3–15 $Å^{-1}$ region, using a Kaiser–Bessel window, and a phase correction applied.

Density functional theory (DFT) was employed to determine the scattering paths within the PMA cluster for the endmember states (reduced and oxidised) investigated in this work. Geometric relaxation calculations were performed using the DFT software package QUANTUM ESPRESSO. Spin-polarised DFT simulations of the electronic structure of the Mo POM were carried out using QUANTUM ESPRESSO v. 7.4.1 *via* the PW.X package.[34,35] QUANTUM ESPRESSO implements DFT within the pseudopotential and plane-wave approaches. A kinetic energy cut-off of 110 Ry (1497 eV) was imposed on the plane-wave basis set for the Kohn–Sham wavefunctions and 1100 Ry (14 966 eV) for the electronic

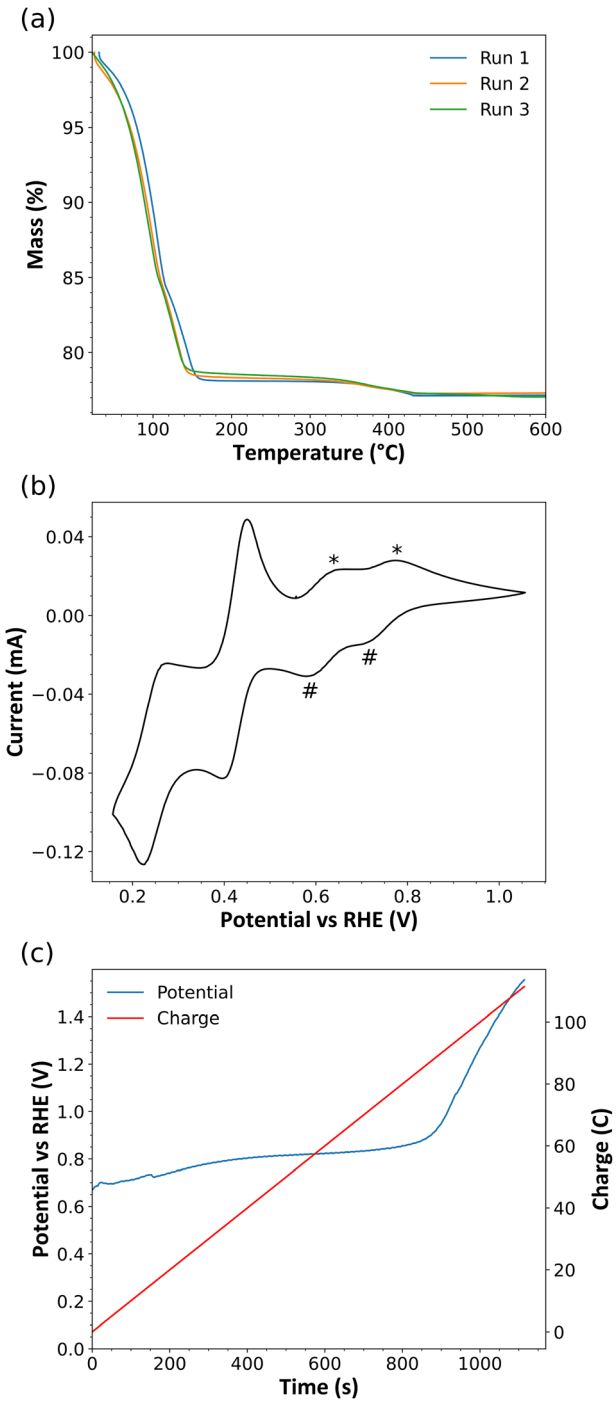

Fig. 3 a) Triplicate TGA data for $H_3[PMo_{12}O_{40}]{\cdot}xH_2O$, b) cyclic voltammogram of PMA collected at 10 mV s^{-1} indicating the reduction (#) and oxidation (*) peaks associated with redox cycling of this material in aqueous solution, c) a plot of operating potential (*versus* RHE) and charge passed as a function of time during re-oxidation of a reduced PMA solution, showing sustained hydrogen generation at <0.85 V *vs.* RHE due to POM-mediated electrolysis before rising sharply when fully discharged.

density. Electron exchange–correlation effects were treated using the Perdew–Burke–Ernzerhof generalized gradient approximation.[36] The first Brillouin zone was sampled at the Γ-point only; the dimensions of the cubic unit cell ($|a|$ = 23.813 Å) were constructed such that there were at least 13 Å of vacuum separation between periodic images. Moreover, to account for periodic boundary conditions, Martyna–Tuckerman corrections were applied to the energy and potential.[37] The stoichiometry of the system investigated was $[PMo_{12}O_{40}]$, to which a total charge of −3 electrons and 0 electrons was applied, which approximates the before and after structures of PMA for use in the Artemis EXAFS modelling. For convergence of the self-consistent cycle, a Gaussian smearing of 68 meV to the electronic occupations was applied, while the crystal structure was relaxed with the Broyden–Fletcher–Goldfarb–Shanno quasi-Newton algorithm. Once a force tolerance of 1.3×10^{-3} atomic units was reached, the structure was deemed to be relaxed. The ultra-soft pseudopotentials Mo.pbe-spn-rrjkus_gipaw.UPF, O.pbe-n-rrkjus_gipaw.UPF and P.pbe-n-rrkjus_gipaw.UPF, from A. Dalcorso's PSlibrary version 1.0.0, were employed.[38]

Modelling of the EXAFS spectra of each of the determined structures was performed using Artemis software with a *K*-range of 3.3–14.8 Å and a *R*-range of 1.0–3.5 Å. Spectra were background corrected but not phase corrected.

2.3.3 Flow cell electrolysis procedure. A dual-channel peristaltic pump, calibrated to a flow rate 100 cm^3 min^{-1}, was used to circulate the reduced PMA solution and 0.5 mol dm^{-3} H_2SO_4 through the anode and cathode compartments of the flow cell, respectively. A sequence of electrochemical steps was then carried out using an Autolab PGSTAT204 potentiostat and Nova 2.1 software, as follows: (i) open-circuit potential (OCP) was determined for 30 s; (ii) galvanostatic electrolysis at 0.1 A held until the cell reached a cell voltage limit of 1.0 V; (iii) potentiostatic measurement at 1.0 V until the cell current decreased below 0.003 A and (iv) final OCP determination.

2.3.4 Mass spectrometry. The remaining port on each of the anolyte and catholyte reservoirs was connected to a Pfeiffer Omnistar 1.0 and an ESS Ecocat mass spectrometer, respectively, for analysis of the off-gases from each compartment. A flow of 2 cm^3 min^{-1} Ar was employed as carrier gas and air was drawn in through an exhaust in order to ensure the correct gas flow rate for the mass spectrometers.

3. Results and discussion

3.1 Physical characterisation of $H_3[PMo_{12}O_{40}]$

In order to accurately determine the concentration of the PMA solutions produced from the yellow, crystalline solid received from the manufacturer, thermogravimetric analysis (TGA) of this material was performed to determine the amount of water of crystallisation present in the structure of this very hygroscopic material. Fig. 3a displays this TGA data in the form of percentage mass loss as a function of temperature. Three experiments were performed using two different instruments to verify water content and the formula of this compound was determined to be: $H_3[PMo_{12}O_{40}]{\cdot}27.2H_2O$.

Table 1 Details of materials used as standards for XAS analysis and the quantities of active material/cellulose matrix used to make each pellet

Standard material	Purity/supplier	Mass of standard/mg	Mass of cellulose/mg
MoO_3	Sigma-Aldrich	24.30	56.71
MoO_2	Sigma-Aldrich	21.66	58.34

3.2 Electrochemical evaluation of PEM electrolysers operating with reduced PMA anolytes

The cyclic voltammetry conducted on PMA (at pH = 0.8) is shown in Fig. 3b, with the oxidation and reduction potentials of the first two redox peaks noted. This data aligns well with previously reported work[15] and shows that variation of the concentration of PMA does not affect the observed redox peaks. It is widely assumed that this anionic charge is delocalised across the oxide framework in the Keggin structure, but to our knowledge no aqueous XAS experiments have been carried out to verify this until the present study.[39–41] Utilising the redox potentials identified in the CV data (Fig. 3b), electrochemical reduction (0.506 V *vs.* RHE) and oxidation (0.947 V *vs.* RHE) operations were carried out in an H-cell and are shown in Fig. S4. These experiments demonstrate the electrochemical behaviour of PMA without any potential interference from the biomass-based reducing agents and allows comparison of the extent of reduction/oxidation when biomass is the only source of reduction for PMA. The reduction current shows a distinct plateau (between 2000 and 4000 seconds) which could be indicative of two 1-electron processes.

To showcase the unique selling point of the redox mediated electrolysis process, a further experiment was conducted to illustrate the lower potential required to conduct electrolysis under these conditions as compared to water electrolysis, which typically occurs around 1.6 V. Fig. 3c provides an example of how the potential varies as the redox mediator is electrochemically oxidised from the fully reduced to fully oxidised state. When the current is held at 0.1 A, the potential needed to oxidise the PMA is between 0.65 V and 0.85 V *vs.* RHE. Once most of the charge held within the PMA has been removed (approximately 90 C), the potential starts to rise above 0.9 V rapidly, as there is now less reduced PMA available to oxidise and the system starts to oxidise water instead. This is shown due to the rapid increase from 0.9 V (the oxidation potential of PMA) to >1.5 V (well into the region of water oxidation) at 0.1 A.

3.3 Thermal digestion of biomass and determining extent of reduction

The biomass samples (both lignin and draff) were thermally digested according to previously reported work,[15] to prepare samples of reduced PMA. In addition, an electrochemically reduced PMA solution (containing no biomass) was produced to provide a reference data set. Based upon the re-oxidation experiments performed during XAS experiments, the charge passed for each reduced PMA solution (electrochemically, lignin or draff-reduced) was calculated, with respect to the concentration and volume used. As the sample without biomass was electrochemically reduced to 100% (with respect to the first 2-electron process observed in the CV data), this sample was used as a baseline to determine the reduction extents of the lignin and draff-reduced samples. A summary of the average reduction extents from all experiments performed during XAS is provided in Table 2 and the corresponding electrochemical data is presented in section 3.4.

Lignin displays a high average reduction extent (85.1%), proving to be a good standard to compare other waste biomass sources to for this digestion process. In addition, the three samples that were available during the operando experiments all exhibited consistent reduction extents. Draff digestion, by comparison, resulted in a lower reduction extent (48.0%); around half the reduction extent compared with purely electrochemical reduction, but demonstrating similar results to previous work exemplifying the reproducibility of the thermal digestion process.[15] As draff comprises 80% by weight (wt%) water, 4 wt% cellulose, 5% hemi-cellulose, 3 wt% protein, 5 wt% Lignin, 2 wt% ash and 1 wt% residual starch, and lignin is known to be more readily digested by PMA than cellulosic materials, the lower reduction extent of draff, even at comparable dry loading of biomass, is expected.[42,43] In addition, native biomass digestion performed by other researchers leads to similar extent of reduction to those determined in this work.[20]

3.4 Operando XAS analysis of PMA during electrolysis

In order to probe the changes in oxidation state of the Mo-centres within the PMA, as well as the local chemical structure of the catalyst, a PEM electrolysis cell was operated whilst synchrotron XAS measurements were collected. Aliquots of the same reduced PMA solutions used in the three-electrode electrochemical evaluations were employed for these operando XAS experiments, though two-electrode measurements were performed in this instance, due to setup limitations during the experimental period.

Table 2 Average charge and reduction extent observed with various reduction methods of PMA

Sample (reduced PMA)	Charge (C)	Reduction extent (%)
Electrochemically	213.7	100.0
Lignin	181.9	85.1
Draff	102.5	48.0

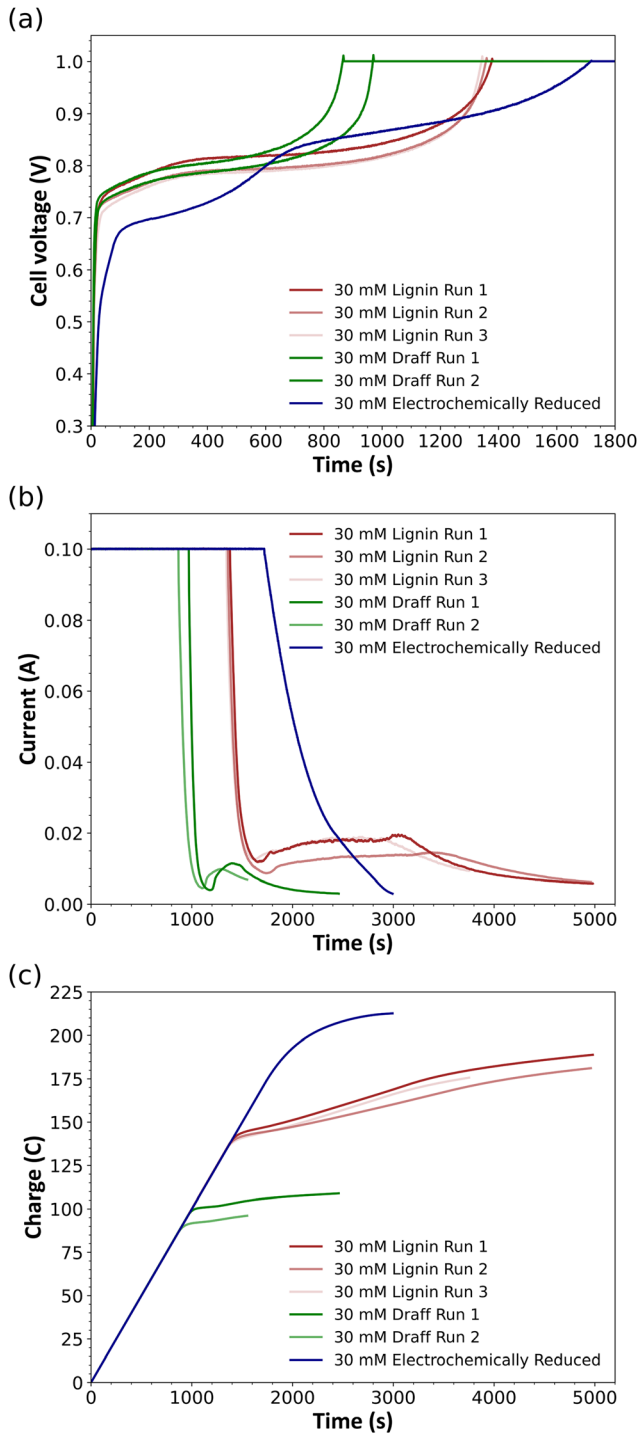

Fig. 4 Electrochemical data from operando XAS experiments: a) voltage *vs.* time, b) current *vs.* time and c) cumulative charge *vs.* time for oxidation in a PEM electrolysis cell using a 0.03 mol dm^{-3} reduced PMA anolyte, a 0.5 mol dm^{-3} $H_2SO_{4(aq)}$ catholyte at 25 °C.

Fig. 4 displays electrochemical data collected for the PEM electrolyser during this operando experiment including (a) cell voltage, (b) current and (c) cumulative charge *versus* time. Initially the PEM was operated in galvanostatic mode at a current of 0.1 A to reoxidise the PMA catalyst, whilst capturing changes in the Mo K-edge of the Mo centres within the POM structure. The voltage can be seen to increase under galvanostatic conditions which confirms that reoxidation occurred readily. The data for the electrochemically reduced sample shows the presence of two 1-electron processes (at ~0.70 V and ~0.85 V *vs.* counter) that are expected in this voltage range for the PMA catalyst; the two-electron redox shuttling between $[PMo_{12}O_{40}]^{5-}$ and $[PMo_{12}O_{40}]^{3-}$ being the mechanism accessed for this POM-mediated electrolysis. However, for the reduced PMA solutions resulting from thermal biomass digestion, it is interesting to note that there is only one diffuse peak, possibly representing a single two-electron process (between 0.70 V and 0.85 V), before the voltage increases sharply towards the 1.0 V cutoff. This could be explained by the fact that the PMA solutions that were exposed to thermal digestion of biomass were less than 100% reduced, which may result in a less prominent second reduction peak (due to a lower concentration of reduced PMA being present in solution) which is convolved with the prominent first reduction peak.

Once a critical value of 1.0 V was achieved, operation switched to potentiostatic mode (held at 1.0 V) until the current response dropped to a critically low value (<0.003 A), which indicated that the reoxidation process was complete. Again, a clear difference in the current profile of the electrochemically reduced PMA and the thermally digested PMA solutions can be identified. In the case of the electrochemically reduced PMA, the current declines from 0.10 A to ~0.003 A between 1700 and 2990 s (Fig. 4b). In comparison, all PMA samples reduced by thermal digestion of draff and lignin show a much more rapid drop in current (~900–1200 s and ~1500–1700 s, respectively), before exhibiting a small increase in current output. Although the rapid decline of current, after switching to potentiostatic operation, is expected in the draff and lignin samples (due to the lower extent of reduction and, therefore, shorter time for reoxidation), the uptick in current passage could relate to direct, electrochemical oxidation of any remaining soluble biomass in the PMA anolyte at these higher voltages as there is a clear absence of any such processes in the current *vs.* time plots of any of the electrochemically reduced PMA samples presented in this work. In addition to these features, there appears to be good reproducibility between draff samples and lignin samples, especially as new MEAs were employed for each experiment.

Furthermore, the cumulative charge *vs.* time plots presented in Fig. 4c show a distinct difference between the profiles of electrochemically reduced and biomass reduced PMA solutions. The former exhibits strong linearity throughout the main part of the experiment, followed by a gradual increase in charge passed (indicated by the curvature of this data series) as the reoxidation reaches the terminal stages. In comparison, the latter demonstrates a sharp reduction in the rate of charge passing, corroborating the aforementioned observations.

3.5 Operando mass spectrometry analysis

Fig. 5 displays mass spectra for the anode and cathode chamber exhausts as a function of operational time (note the differences in experiment duration) displaying recorded traces for H_2, O_2

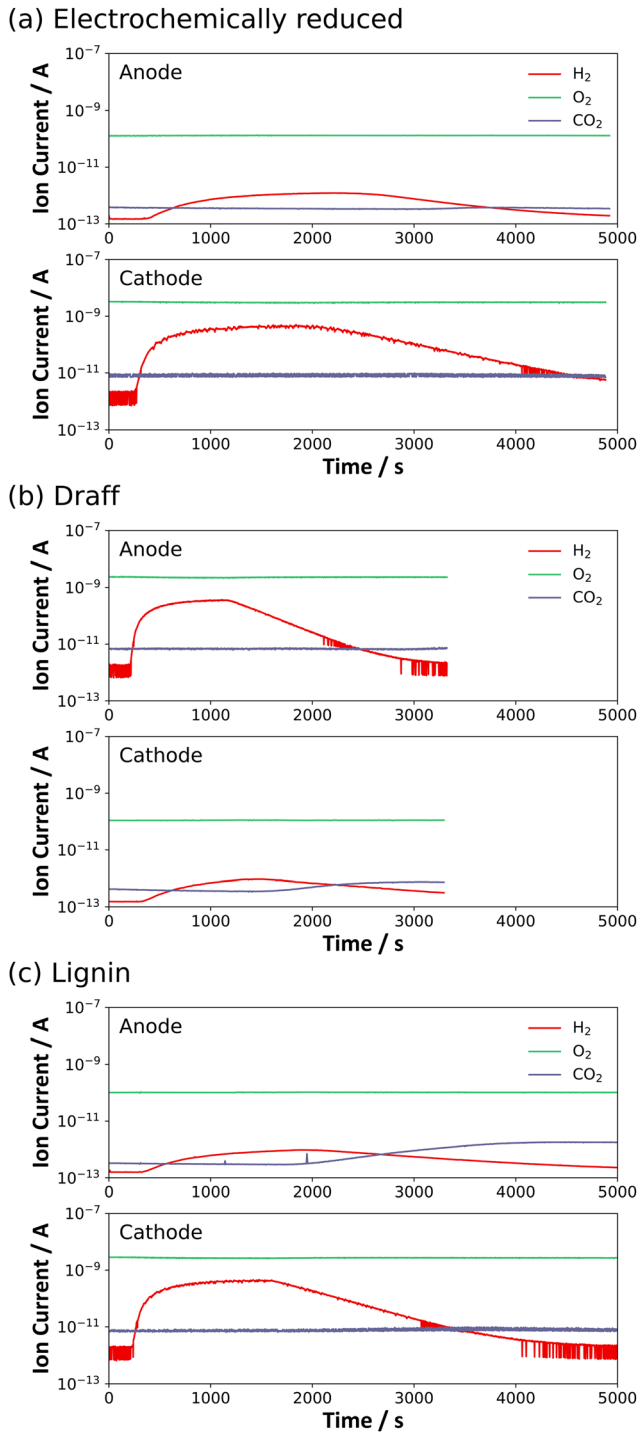

Fig. 5 Mass spectrometric data of anode and cathode chamber exhaust gases for operando XAS experiments utilising PMA solutions reduced a) electrochemically, b) *via* thermal digestion of draff (run 1) and c) *via* thermal digestion of lignin (run 1).

and CO_2. Additional traces for N_2, H_2O and Ar were recorded but showed a stable ion current throughout and are omitted for clarity of the figures. First to note, regardless of the method used to reduce the PMA solutions, each experiment indicated that hydrogen production clearly occurs at the cathode, but there is also a back-diffusion of hydrogen through the PEM to the anode, known as 'crossover' in this field of research.[44] Experimental conditions, such as concentration of anolyte and catholyte, pressure, flow rate and current/voltage of operation, should be modified in future work to minimise this crossover phenomenon to ensure that the majority of hydrogen can be collected from the cathode compartment for simpler system design. In PEM water electrolysers, crossover of hydrogen back into the anode compartment, where oxygen evolves, can cause significant safety issues, unless operational procedures are implemented to reduce this crossover phenomenon.[44] As no oxygen evolution occurs in this mediated electrolysis system, the phenomenon of crossover poses less of a safety concern and offers a direct benefit over state-of-the-art PEM water electrolysers. In addition, for the electrolysers operating on biomass reduced PMA anolytes (*i.e.* draff run 1 and lignin run 1), after the plateaux of hydrogen production are reached and begin to wane, an increase in carbon dioxide production is observed in the anode compartment (Fig. 5b and c). As PMA is a highly corrosive species, the release of carbon dioxide could relate to oxidation of the carbon paper and felt of the electrodes, however, as shown by Fig. 5a, the analogous region of the mass spectra for the electrochemically reduced PMA shows a negligible increase in carbon dioxide concentration. Although there is a time delay between the electrochemical oxidation of the PMA solutions and the gas analysis (due to the low flow rate required by the mass spectrometers employed), the uptick in current passage, observed only for the biomass-containing solutions in Fig. 4b, appears to relate to the evolution of carbon dioxide in the corresponding mass spectra. Therefore, this increase in carbon dioxide evolution could relate to direct oxidation of residual biomass that is soluble in the PMA solution, which is consistent with observations in the literature.[45] This 'direct' biomass oxidation results in additional charge passage to the re-oxidation of the reduced PMA solution, providing an explanation for the origin of the higher charge than expected from the lignin and draff solutions.

3.6 Correlation of XAS data with PMA state of charge

Fig. 6a displays X-ray absorption spectra for the Mo K-edge of MoO_2 and MoO_3 standard materials and additional spectra from other relevant standard materials are shown in SI Fig. S2, all of which are comparable to those presented in the literature.[46–48] Spectra of pre- and post-electrolysis (reduced and oxidised, respectively) 0.03 mol dm^{-3} electrochemically treated, lignin-digested or draff-digested PMA solutions are also plotted in Fig. 6a for comparison to the standards. As expected, the solid-state (shown in Fig. S2) and liquid-state fully oxidised PMA samples exhibit a maximum in the first derivative of the absorption coefficient (20 017 eV) almost identical to that of MoO_3 (20 016.9 eV), indicating that the Mo centres in these materials most likely have a formal oxidation state of VI. Interestingly, only a small change in the Mo K-edge position is observed between the fully oxidised and fully reduced liquid PMA samples, as indicated by the comparative plot in Fig. 6a. However, the shoulder peak at

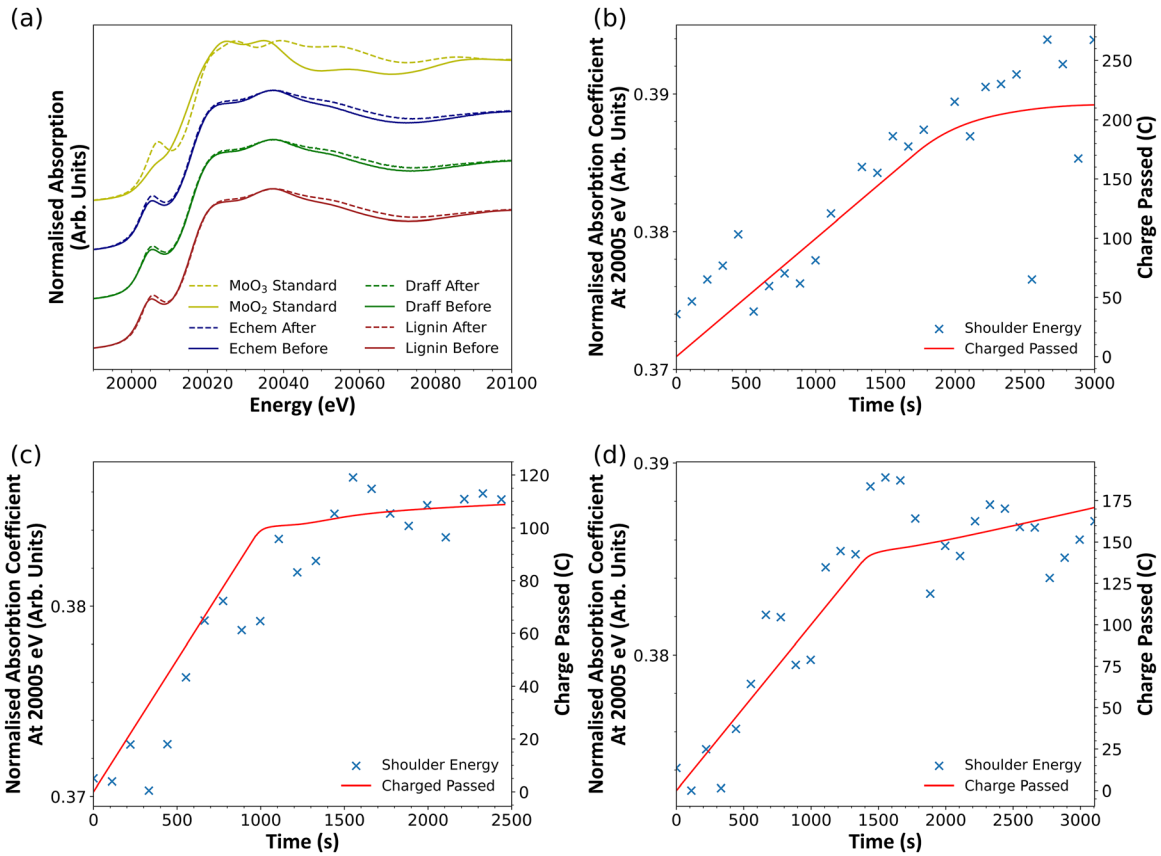

Fig. 6 (a) XANES spectra before and after reoxidation of reduced PMA solutions compared with MoO_3 and MoO_2 standards. (b–d) XANES energy of shoulder peak (~20 005 eV) and charge passed *vs.* time for b) electrochemical, c) draff and d) lignin reduced PMA.

20 005 eV exhibits an increase in amplitude in the reduced state, whilst the extended X-ray absorption fine structure (EXAFS) region (Fig. 7, further discussed below) shows changes in the second and third shells, implying that although some structural rearrangement of the Mo-centre network occurs within this material, dispersal of charge throughout the whole structure is likely.

Considering the change in oxidation state of the Mo centres, Fig. 6(b–d) shows the normalised absorption coefficient of the pre-edge feature in the XANES region (at 20 005 eV), overlaid with the charge passed, as a function of time during the operando PEM electrolysis measurements. Fig. 6b–d show data traces for electrochemical, draff (run 1) and lignin (run 1) samples, respectively. All data series (including those displayed previously in Fig. 4) show two different rates of charge passage which correlate directly to the operational mode employed; i) a faster rate with a steeper gradient observed during galvanostatic operation at 0.1 A (until the 1.0 V cutoff was reached) and ii) a slower rate with a shallower gradient relating to potentiostatic operation at 1.0 V. The increase in normalised absorption coefficient that accompanies charge passage indicates that a small shift in the peak position of the Mo K-edge, and consequently oxidation state, occurs and relates to partial re-oxidation of the Mo centres of the PMA structure, whereas the difference in amplitude of the shoulder peak (displayed in Fig. 6a), may relate to changes in symmetry of the structure of the material. The changes in normalised absorption coefficient match the charge passage behaviour of POM-mediated PEM electrolysers well, with the electrochemically reduced sample showing a more gradual increase in coefficient after switching to potentiostatic mode, in comparison to a sharp reduction in the rate of change of this coefficient for the biomass-reduced samples.

Though this is the first report of XAS performed upon PMA in the aqueous state, important information on the structural rearrangements that this material might undergo can be found in the solid-state XAS literature. In particular, work by Wang *et al.* suggested that when incorporating the $TBA_3[PMo_{12}O_{40}]$ material into the cathode of a LIB, each Mo centre was reduced from Mo^{6+} to Mo^{4+}, corresponding to a 24-electron reduction. In this case, the polyanion was reduced from $[PMo_{12}O_{40}]^{3-}$ to $[PMo_{12}O_{40}]^{27-}$, resulting in the formation of new Mo^{4+} triangles within the structure.[30] This was confirmed by Falbo *et al.* whose DFT studies indicated that significant structural changes did not occur within the polyanion until each Mo centre had been reduced by 1 electron (*i.e.* forming $[PMo_{12}O_{40}]^{15-}$), at which point Mo^{5+} centres would exist.[49] In addition, the existence of individual Mo^{5+} centres[49–52] within hybrid POMs, *e.g.* mixed molybdenum-tungsten Keggin-type POMs,[50] has been shown. However, given that a relatively mild two-electron reduction was

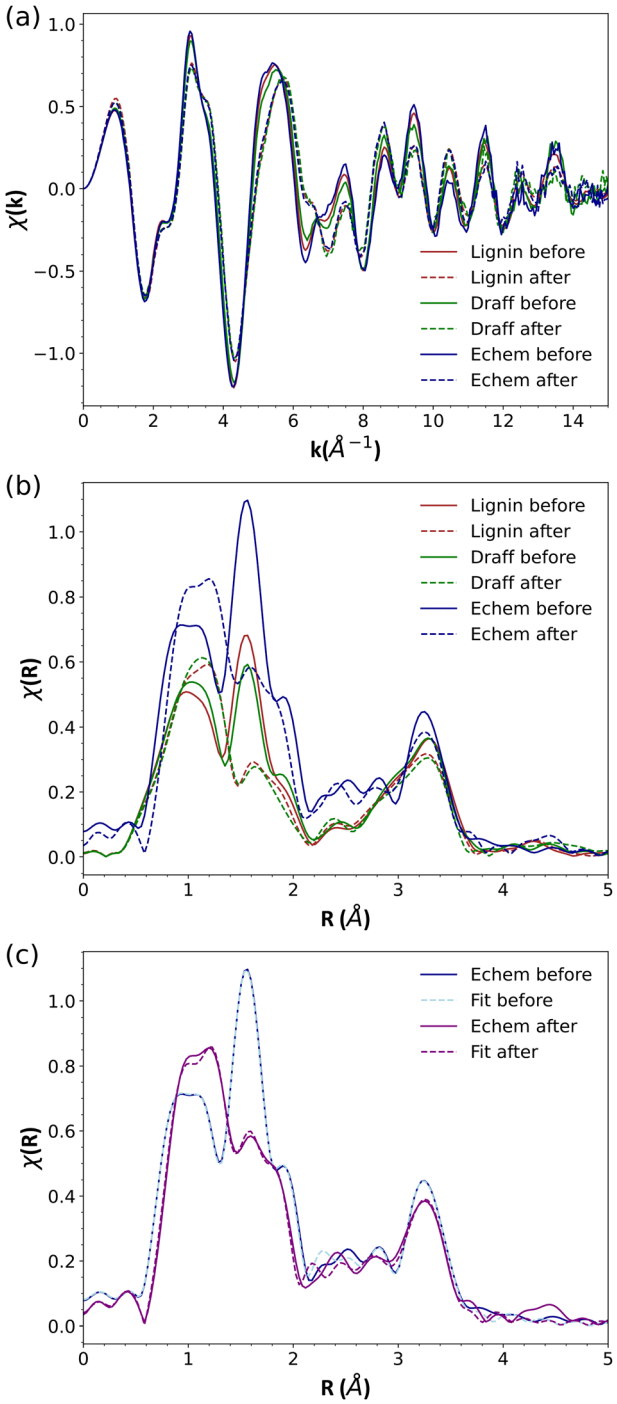

Fig. 7 EXAFS plots collected before and after reoxidation of a variety reduced PMA solutions (a) k^2-weighted EXAFS spectra in k-space and (b) the forward Fourier transform (FFT) over the k = 3.3–15 Å^{-1} region, using a Kaiser–Bessel window, and a phase correction applied, in R-space and (c) before and after R-space plots for the electrochemically reduced and oxidised PMA samples, fitted using simulated X-ray absorption spectra derived from DFT calculations.

performed during the current work, it is unlikely that such an extensive structural rearrangement occurred.

Fig. 7a and b display the K-space and R-space plots of the EXAFS region before and after electrolysis of the electrochemically-reduced, lignin-reduced and draff-reduced PMA solutions. The peak at ~1.8 Å is an amalgam of scattering responses from Mo═O double and Mo–O single bonds, whilst those found between 3–4 Å relate to Mo–Mo bonds. Considering the PMA solutions before electrolysis, the reduction extent follows the order: electrochemically reduced > lignin-reduced > draff reduced. This is reflected in the data displayed in Fig. 7 and indicates that as the extent of reduction increases, the amplitude of the peak ~1.8 Å increases corresponding to a lengthening of these axial Mo═O and bridging Mo–O bonds. In order to provide more accurate information on the structure of the reduced and oxidised, liquid phase PMA, DFT calculations were performed on a $[PMo_{12}O_{40}]$ structure with charges associated with 3 electrons and 0 electrons applied, respectively. The simulated structural information was used to fit experimental XAS data collected for the electrochemically-treated samples (Fig. 7c) and lignin and draff-reduced samples (Fig. S6) using Artemis, allowing bond lengths and coordination numbers to be determined for each of the aforementioned samples before and after electrolysis. This data, including R-factors, is summarised in Table 3 and corroborates the aforementioned observation. Here, the Mo–O2 bond lengths (representing one type of bridging oxygen between Mo centres) clearly shorten upon oxidation, along with the Mo═O1 bond lengths (representing the 'capping' Mo═O bonds in the axial positions of the PMA cluster), with the exception of the Mo═O1 bond for the electrochemically treated sample which lengthens, but is within error. The Mo–O3 and Mo–O4 bonds also generally decrease in length. This, therefore, implies that charge distribution does indeed occur throughout the Mo–O skeleton of the PMA cluster rather than directly at Mo centres and that the relative reduction extent of the PMA solutions under investigation can be observed using XAS, offering an additional method for verification for degree of reduction in these mediator systems.

4. Conclusions

In this research, a promising route for decoupled hydrogen production using a redox cycle- and thermally-stable polyoxometalate catalytic mediator, phosphomolybdic acid ($H_3[PMo_{12}O_{40}]$ or PMA), was investigated in a bespoke proton exchange membrane (PEM) electrolysis cell. Building upon the authors' previous work, it has been demonstrated that waste biomass sources including lignin and draff (spent grains from a whisky distillery) can be thermally digested by PMA in aqueous solution, reducing the mediator with respect to the first 2-electron process identified during cyclic voltammetry. This reduction process is the result of abstraction of protons and electrons from (*i.e.* oxidation of) the biomass. Subsequently, use of the reduced PMA solution as the anolyte during PEM electrolysis experiments indicated that upon application of an electrolysis current, the PMA could be reoxidised at around 0.8 V (regenerating the mediator for repeated use), whilst generating green hydrogen when using renewably-generated electricity. This potentially halves the energy requirement for green hydrogen production

Table 3 A summary of bond lengths, coordination numbers (CN) and *R*-factors for before (reduced) and after (oxidised) samples of PMA reduced electrochemically, by lignin digestion and draff digestion

	EChem		Lignin		Draff	
Shell	Before	After oxidation	Before	After oxidation	Before	After oxidation
Mo═O1	1.640(2)	1.643(3)	1.642(3)	1.639(5)	1.626(2)	1.603(3)
CN	1.2(1)	1.0(1)	1.4(2)	1.2(3)	1.5(1)	1.1(2)
$\sigma^2 \times 10^{-3}$	0.4(3)	0.7(6)	1.4(8)	4.1(17)	1.7(6)	1.5(10)
Mo–O2	1.805(1)	1.790(3)	1.796(3)	1.764(8)	1.773(2)	1.733(2)
CN	2.3(1)	2.5(1)	2.3(2)	2.7(2)	2.4(1)	2.1(1)
$\sigma^2 \times 10^{-3}$	1.7(2)	3.4(4)	1.9(5)	5.8(7)	2.2(4)	2.0(5)
Mo–O3	1.945(1)	1.967(4)	1.941(3)	1.939(13)	1.923(3)	1.893(5)
CN	2.4(1)	2.1(2)	2.4(2)	2.0(2)	2.1(2)	1.9(3)
$\sigma^2 \times 10^{-3}$	1.3(3)	5.4(8)	1.6(6)	5.8(7)	1.4(5)	5.0(14)
Mo–O4	2.404(5)	2.371(13)	2.396(11)	2.380(17)	2.375(7)	2.353(14)
CN	1.0(2)	0.8(3)	0.9(2)	0.7(2)	1.2(1)	1.0(4)
$\sigma^2 \times 10^{-3}$	2.5(11)	3.9(36)	1.6(12)	2.0(17)	2.2(7)	4.2(14)
Mo–Mo1	3.436(2)	3.413(4)	3.447(5)	3.451(6)	3.372(3)	3.435(6)
CN	1.8(2)	1.7(2)	2.0(5)	2.0(4)	2.0(3)	2.4(6)
$\sigma^2 \times 10^{-3}$	4.1(5)	5.9(8)	4.7(13)	3.2(8)	4.7(8)	6.7(15)
Mo–Mo2	3.765(7)	3.608(13)	3.779(10)	3.753(12)	3.727(5)	3.717(10)
CN	2.3(5)	2.3(3)	2.7(13)	2.4(5)	2.2(5)	2.6(10)
$\sigma^2 \times 10^{-3}$	10.8(17)	15.0(20)	8.9(29)	7.7(19)	5.8(11)	9.1(26)
E0	5.8(1)	5.9(2)	5.8(4)	4.9(4)	2.1(3)	0.9(4)
$S0^2$	0.96(1)	0.96(1)	0.96(3)	0.98(3)	0.96(2)	0.96(3)
r-Factor $\times 10^{-3}$	1.38	5.96	15.17	16.11	10.64	11.86

when compared to water electrolysis whilst also valorising underutilised waste biomass streams.

The authors report the successful design, construction and operation of a bespoke PEM flow cell to enable the first *operando* electrolysis X-ray absorption spectroscopy (XAS) experiment to gain insight into the behaviour of aqueous PMA under operating conditions. These experiments allowed the change in oxidation state of the Mo-centres within the $[PMo_{12}O_{40}]^{3-/5-}$ structure to be probed as a function of charge passed (reoxidation), through monitoring of the Mo K-edge position, and indicated that only a minor shift in Mo K-edge position was observed upon reoxidation. This infers that charge may be more widely distributed throughout the entire structure rather than solely between the 12 Mo centres. Complementary DFT fitting of EXAFS data confirmed this interpretation, revealing a measurable decrease in Mo–O bond lengths upon reoxidation, consistent with structural contraction and global charge delocalisation across the heteropolyacid framework. Moreover, electrochemical data collected during *operando* XAS experiments indicated that the passage of charge during reoxidation correlated well with the change in oxidation state of the Mo K-edge. Significantly, after the initial galvanostatic operation (0.1 A) of the PEM electrolyser (required to provide a controlled reoxidation rate of the PMA mediator for XAS) and switching to potentiostatic operation (1.0 V), samples reduced through biomass digestion displayed secondary upticks in current passage, whilst those that were reduced electrochemically did not. Mass spectrometry of off gases from the electrolyte vessels confirmed the generation of hydrogen in the cathode compartment. However, some presumed crossover of hydrogen back towards the anode compartment *via* the membrane was observed, which should be minimised, but is not critical to operation here, owing to the lack of oxygen evolution at the anode in this particular system. Interestingly, in biomass reduced samples only, evolution of carbon dioxide was observed, likely corresponding to the aforementioned upticks in current passage and implying that these observations may relate to direct oxidation of biomass in solution.

These findings demonstrate the powerful potential of applying combined *operando* XAS with mass spectrometry and electrochemical analysis and help to establish a foundational methodology for future studies of heteropolyacids in decoupled electrochemical hydrogen production technologies.

Author contributions

Robert Price*: conceptualization, methodology, formal analysis, investigation, writing – original draft. Lewis MacDonald*: investigation, visualization, writing – original draft. Luke L. Keenan*: investigation, formal analysis, resources, writing – review & editing. William Johnson: investigation, visualization, validation. Stephen M. Lyth: investigation, writing – review & editing. Jun Li: funding acquisition, supervision, writing – review & editing. Edward Brightman: conceptualization, data curation, funding acquisition, investigation, methodology, project administration, supervision, writing – review & editing. (*) – these authors share equal first authorship.

Conflicts of interest

There are no conflicts to declare.

Data availability

All data for this article are available at University of Strathclyde at https://doi.org/10.15129/17f08512-ae0a-42e8-be4e-2f816f53da4a.

Supplementary information (SI): showing additional experimental details, voltammetry data and EXAFS fitting data. See DOI: https://doi.org/10.1039/d5cy00763a.

Acknowledgements

The authors would like to thank Mr Liam Kirkwood, Mr Cameron Gemmell (University of Strathclyde) and Mr Sam Embling (Diamond Light Source Ltd.) for design, modification and manufacture of the flow cell setup components for XAS experiments, as well as Dr Joshua D. Elliot (Diamond Light Source Ltd.) for invaluable assistance with DFT simulations. Thanks also go to Dr Zac Dehaney Steven, Dr Douglas Stewart and Dr Ying Yuan of Ames Goldsmith Ceimig for providing Pt-coated porous transport layer coupons. In addition, we thank Mr Alasdair Day and Mr Norman Gillies (R&B Distillers Ltd.) for their support. We gratefully acknowledge funding from the UK Science and Technology Facilities Council (STFC) for beamtime at Diamond Light Source's B18 beamline (SP33569-1), the Engineering and Physical Sciences Research Council *via* the SUPERGEN Bioenergy Impact Hub (EP/Y016300/1) and from Innovate UK *via* KTP no. 13087. Knowledge Transfer Partnerships (KTPs) aim to help businesses improve their competitiveness and productivity through better use of knowledge, technology and skills within the UK knowledge base. This KTP was co-funded by UKRI through Innovate UK and R&B Distillers Ltd.

References

1 V. Masson-Delmotte, P. Zhai, H.-O. Pörtner, D. Roberts, J. Skea, P. R. Shukla, A. Pirani, W. Moufouma-Okia, C. Péan, R. Pidcock, S. Connors, J. B. R. Matthews, Y. Chen, X. Zhou, M. I. Gomis, E. Lonnoy, T. Maycock, M. Tignor and T. Waterfield, *SR15 - Global Warming of 1.5 °C*, 2018.
2 M. Götz, J. Lefebvre, F. Mörs, A. McDaniel Koch, F. Graf, S. Bajohr, R. Reimert and T. Kolb, *Renewable Energy*, 2016, **85**, 1371–1390.
3 J. B. Hansen, *Faraday Discuss.*, 2015, **182**, 9–48.
4 A. Badgett, J. Brauch, A. Thatte, R. Rubin, C. Skangos, X. Wang, R. Ahluwalia, B. Pivovar and M. Ruth, *Updated Manufactured Cost Analysis for Proton Exchange Membrane Water Electrolyzers*, Golden, CO, 2024.
5 D. M. Alonso, S. G. Wettstein and J. A. Dumesic, *Chem. Soc. Rev.*, 2012, **41**, 8075–8098.
6 J. González-Cobos, M. S. Prévot and P. Vernoux, *Curr. Opin. Electrochem.*, 2023, **39**, 101255.
7 W. Wu, X. Y. Wu, S. S. Wang and C. Z. Lu, *ACS Sustainable Chem. Eng.*, 2020, **8**, 18528–18534.
8 S. J. Yim, H. Oh, Y. Choi, G. N. Ahn, C. H. Park, Y. H. Kim, J. Ryu and D. P. Kim, *Adv. Sci.*, 2022, **9**, 2204170.
9 D. L. Long, R. Tsunashima and L. Cronin, *Angew. Chem., Int. Ed.*, 2010, **49**, 1736–1758.
10 M. D. Symes and L. Cronin, *Nat. Chem.*, 2013, **5**, 403–409.
11 L. Macdonald, B. Rausch, M. D. Symes and L. Cronin, *Chem. Commun.*, 2018, **54**, 1093–1096.
12 L. MacDonald, J. C. McGlynn, N. Irvine, I. Alshibane, L. G. Bloor, B. Rausch, J. S. J. Hargreaves and L. Cronin, *Sustainable Energy Fuels*, 2017, **1**, 1782–1787.
13 M. Sadakane and E. Steckhan, *Chem. Rev.*, 1998, **98**, 219–237.
14 B. B. Sarma and R. Neumann, *Nat. Commun.*, 2014, **5**, 1–6.
15 R. Price, L. MacDonald, N. Gillies, A. Day, E. Brightman and J. Li, *Faraday Discuss.*, 2023, **247**, 268–288.
16 Y. Li, W. Liu, Z. Zhang, X. Du, L. Yu and Y. Deng, *Commun. Chem.*, 2019, **2**, 1–9.
17 X. Du, H. Zhang, K. P. Sullivan, P. Gogoi and Y. Deng, *ChemSusChem*, 2020, **13**, 4318–4343.
18 M. Li, T. Wang, M. Zhao and Y. Wang, *Int. J. Hydrogen Energy*, 2022, **47**, 15357–15369.
19 H. Oh, Y. Choi, C. Shin, T. V. T. Nguyen, Y. Han, H. Kim, Y. H. Kim, J. W. Lee, J. W. Jang and J. Ryu, *ACS Catal.*, 2020, **10**, 2060–2068.
20 W. Liu, Y. Cui, X. Du, Z. Zhang, Z. Chao and Y. Deng, *Energy Environ. Sci.*, 2016, **9**, 467–472.
21 F. Sheng, Q. Yang, D. Cui, C. Liu, Y. Sun, X. Wang and W. Su, *Energy Fuels*, 2020, **34**, 10282–10289.
22 S. Ishikawa, T. Ikeda, M. Koutani, S. Yasumura, K. Amakawa, K. Shimoda, Y. Jing, T. Toyao, M. Sadakane, K. I. Shimizu and W. Ueda, *J. Am. Chem. Soc.*, 2022, **144**, 7693–7708.
23 M. H. Tran, H. Ohkita, T. Mizushima and N. Kakuta, *Appl. Catal., A*, 2005, **287**, 129–134.
24 Q. Huynh and J. M. M. Millet, *J. Phys. Chem. Solids*, 2005, **66**, 887–894.
25 L. Cheng, L. Niu, J. Gong and S. Dong, *Chem. Mater.*, 1999, **11**, 1465–1475.
26 B. B. Bardin and R. J. Davis, *Appl. Catal., A*, 1999, **185**, 283–292.
27 P. E. Boahene, S. Vedachalam and A. K. Dalai, *Fuel*, 2022, **317**, 123447.
28 H. Nair, J. T. Miller, E. A. Stach and C. D. Baertsch, *J. Catal.*, 2010, **270**, 40–47.
29 J. Wienold, O. Timpe and T. Ressler, *Chem. – Eur. J.*, 2003, **9**, 6007–6017.
30 H. Wang, S. Hamanaka, Y. Nishimoto, S. Irle, T. Yokoyama, H. Yoshikawa and K. Awaga, *J. Am. Chem. Soc.*, 2012, **134**, 4918–4924.
31 A. J. Dent, G. Cibin, S. Ramos, A. D. Smith, S. M. Scott, L. Varandas, M. R. Pearson, N. A. Krumpa, C. P. Jones and P. E. Robbins, *J. Phys.: Conf. Ser.*, 2009, **190**, 012039.
32 B. Ravel and M. Newville, *J. Synchrotron Radiat.*, 2005, **12**, 537–541.
33 M. Basham, J. Filik, M. T. Wharmby, P. C. Y. Chang, B. el Kassaby, M. Gerring, J. Aishima, K. Levik, B. C. A. Pulford, I. Sikharulidze, D. Sneddon, M. Webber, S. S. Dhesi, F. Maccherozzi, O. Svensson, S. Brockhauser, G. Náray and A. W. Ashton, *J. Synchrotron Radiat.*, 2015, **22**, 853–858.
34 P. Giannozzi, O. Andreussi, T. Brumme, O. Bunau, M. Buongiorno Nardelli, M. Calandra, R. Car, C. Cavazzoni, D.

Ceresoli, M. Cococcioni, N. Colonna, I. Carnimeo, A. Dal Corso, S. De Gironcoli, P. Delugas, R. A. Distasio, A. Ferretti, A. Floris, G. Fratesi, G. Fugallo, R. Gebauer, U. Gerstmann, F. Giustino, T. Gorni, J. Jia, M. Kawamura, H. Y. Ko, A. Kokalj, E. Kücükbenli, M. Lazzeri, M. Marsili, N. Marzari, F. Mauri, N. L. Nguyen, H. V. Nguyen, A. Otero-De-La-Roza, L. Paulatto, S. Poncé, D. Rocca, R. Sabatini, B. Santra, M. Schlipf, A. P. Seitsonen, A. Smogunov, I. Timrov, T. Thonhauser, P. Umari, N. Vast, X. Wu and S. Baroni, *J. Phys.: Condens. Matter*, 2017, **29**, 465901.

35 P. Giannozzi, S. Baroni, N. Bonini, M. Calandra, R. Car, C. Cavazzoni, D. Ceresoli, G. L. Chiarotti, M. Cococcioni, I. Dabo, A. Dal Corso, S. De Gironcoli, S. Fabris, G. Fratesi, R. Gebauer, U. Gerstmann, C. Gougoussis, A. Kokalj, M. Lazzeri, L. Martin-Samos, N. Marzari, F. Mauri, R. Mazzarello, S. Paolini, A. Pasquarello, L. Paulatto, C. Sbraccia, S. Scandolo, G. Sclauzero, A. P. Seitsonen, A. Smogunov, P. Umari and R. M. Wentzcovitch, *J. Phys.: Condens. Matter*, 2009, **21**, 395502.

36 J. P. Perdew, K. Burke and M. Ernzerhof, *Phys. Rev. Lett.*, 1996, **77**, 3865.

37 G. J. Martyna and M. E. Tuckerman, *J. Chem. Phys.*, 1999, **110**, 2810–2821.

38 A. Dal Corso, *Comput. Mater. Sci.*, 2014, **95**, 337–350.

39 J. M. Maestre, X. Lopez, C. Bo, J.-M. Poblet and N. Casañ-Pastor, *J. Am. Chem. Soc.*, 2001, **123**, 3749–3758.

40 R. A. Prados, P. T. Meiklejohn and M. T. Pope, *J. Am. Chem. Soc.*, 1974, **96**, 1261–1263.

41 P. A. Aparicio, J. M. Poblet and X. Lõpez, *Eur. J. Inorg. Chem.*, 2013, 1910–1916.

42 J. C. Akunna and G. M. Walker, in *The alcohol textbook: a reference for the beverage, fuel and industrial alcohol industries*, ed. G. M. Walker, C. Abbas, W. M. Ingledew and C. Pilgrim, Lallemand Biofuels & Distilled Spirits, Duluth, Georgia, 2017, pp. 529–537.

43 S. I. Mussatto, G. Dragone and I. C. Roberto, *J. Cereal Sci.*, 2006, **43**, 1–14.

44 R. Omrani and B. Shabani, *Electrochim. Acta*, 2021, **377**, 138085.

45 X. Du, W. Liu, Z. Zhang, A. Mulyadi, A. Brittain, J. Gong and Y. Deng, *ChemSusChem*, 2017, **10**, 847–854.

46 V. A. Schoepfer and M. B. J. Lindsay, *Data Brief*, 2022, **45**, 108576.

47 M. Rentería, A. Traverse, O. A. Anunziata, E. J. Lede, L. Pierella and F. G. Requejo, *J. Synchrotron Radiat.*, 2001, **8**, 631–633.

48 C. T. J. Mensch, J. A. R. Van Veen, B. Van Wingerden and P. Van Dijk, *J. Phys. Chem.*, 1988, **92**, 4961–4964.

49 E. Falbo, C. D. Rankine and T. J. Penfold, *Chem. Phys. Lett.*, 2021, **780**, 138893.

50 M. Laurans, M. Mattera, R. Salles, L. K'Bidi, P. Gouzerh, S. Renaudineau, F. Volatron, G. Guillemot, S. Blanchard, G. Izzet, A. Solé-Daura, J. M. Poblet and A. Proust, *Inorg. Chem.*, 2022, **61**, 7700–7709.

51 T. Matsuyama, S. Kikkawa, N. Kawamura, K. Higashi and S. Yamazoe, *Radiat. Phys. Chem.*, 2024, **215**, 111351.

52 Z. S. Peng, Y. L. Huang, S. Z. Lü, J. T. Tang, T. J. Cai and Q. Deng, *Synth. React. Inorg., Met.-Org., Nano-Met. Chem.*, 2014, **44**, 376–382.

